Scale interactions and scaling laws in rotating flows at moderate Rossby numbers and large Reynolds numbers

P.D. Mininni[1,2], A. Alexakis[3], and A. Pouquet[2]
[1] *Departamento de Física, Facultad de Ciencias Exactas y Naturales, Universidad de Buenos Aires, Ciudad Universitaria, 1428 Buenos Aires, Argentina.*
[2] *NCAR, P.O. Box 3000, Boulder, Colorado 80307-3000, U.S.A.*
[3] *Laboratoire Cassiopée, Observatoire de la Côte d'Azur, BP 4229, Nice Cedex 04, France.*
(Dated: August 18, 2008)

The effect of rotation is considered to become important when the Rossby number is sufficiently small, as is the case in many geophysical and astrophysical flows. Here we present direct numerical simulations to study the effect of rotation in flows with moderate Rossby numbers (down to $Ro \approx 0.07$) but at Reynolds numbers large enough to observe the beginning of a turbulent scaling at scales smaller than the energy injection scale. We use coherent forcing at intermediate scales, leaving enough room in the spectral space for an inverse cascade of energy to also develop. We analyze the spectral behavior of the simulations, the shell-to-shell energy transfer, scaling laws and intermittency, as well as the geometry and the anisotropy of the structures in the flow. At late times, the direct transfer of energy at small scales is mediated by interactions with the largest scale in the system, the energy containing eddies with $k_\perp \approx 1$, where $\perp$ refers to wavevectors perpendicular the axis of rotation. The transfer between modes with wavevector parallel to the rotation is strongly quenched. The inverse cascade of energy at scales larger than the energy injection scale is non-local, and energy is transferred directly from small scales to the largest available scale. We observe both a direct and inverse cascade of energy at high rotation rate, indicative that these cascades can take place simultaneously. Also, as time evolves and the energy piles up at the large scales, the intermittency of the direct cascade of energy is preserved while corrections due to intermittency are found to be the same (within error bars) as in homogeneous non-rotating turbulence.

I. INTRODUCTION

Strong rotation is present in many geophysical and astrophysical flows. Its effect is considered to become important when the Rossby number (the ratio of the convective to the Coriolis acceleration, or the ratio of the rotation period to the eddy turn over time) is sufficiently small. The large scales of atmospheric and oceanic flows for example are affected by the rotation of the Earth. The Rossby number for mid-latitude synoptic scales in the atmosphere is $Ro \approx 0.1$ [46]. In the Sun, the typical Rossby number in the convective zone is $Ro \approx 0.1 - 1$ [35]. Furthermore, the Reynolds number (Re, the ratio of the convective to the viscous acceleration) in these systems is also very large, and the flows are in a turbulent state.

Many studies have considered solely the effect of rotation in a turbulent flow, as a first step to gain better understanding of the fluid dynamics of geophysical systems, for which, e.g., stratification also plays an important role. For rapid rotation (very small Rossby numbers), significant progress has been made by applying resonant wave theory [26, 57], two-point spectral closures [15, 16], and weak turbulence theory [25]. In these approaches, the flow is considered as a superposition of inertial waves with a short period, and the evolution of the system for long times is derived considering the effect of resonant triad interactions.

Recently, resonant wave theory has been shown to correspond to an asymptotic limit for a general class of geophysical flows with wave dynamics [7, 23]. Also, the connection between resonant wave theory and two-point closures based on helical modes [15, 57] was shown in Ref. [10]. This approach sheds light on the mechanism that drives the flow to be quasi-two dimensional at large scales [15, 57]: energy in three dimensional modes is transferred by a subset of the resonant interactions to modes with smaller vertical wavenumber. It also explains successfully the observed enhanced transfer of energy from the small to the large scales [52].

In fact, it is well known that the theory of weak turbulence is only valid when the wave period (the rotation period here) is much shorter than the eddy turnover time at all scales. For large Reynolds numbers, small scales are excited with a characteristic timescale proportional to the eddy turnover time, that decreases as the scales become smaller. Therefore the approximations made in such theories can break down at sufficiently small scales, provided that the Reynolds number is large enough for these scales to be excited. How the results of resonant wave theory extend to the case of only moderate Rossby numbers but very large Reynolds numbers is still unclear. Two-point spectral closures [15, 16] can be used to match the two regimes using the same theoretical tool (see e.g., [10]). This shows that the energy transfer is anisotropic even at moderate Rossby numbers because of linear phase-mixing, and that resonant triads are selected in the limit of small Rossby number (see also [54, 56]).

Another approach for understanding rotating flows at large Reynolds numbers is to develop phenomenological models based on scaling arguments and self-similarity. Initial phenomenological investigations con-

sidered isotropic energy spectra $E(k)$ [60, 61] that suggested the power-law behavior $E(k) \sim k^{-2}$ provided that the examined wavenumbers were smaller than a critical wave number $k_\Omega \sim \sqrt{\Omega^3/\epsilon}$, where ϵ is the energy dissipation rate. For larger wavenumbers, the energy spectrum transitioned to the isotropic Kolmogorov energy spectrum $E(k) \sim k^{-5/3}$. Anisotropy was taken into account in phenomenological models in [17], where it was recognized that a considerable amount of the energy will be confined in "quasi-2D" modes. An anisotropic energy spectrum $E(k) \sim k_\perp^{-2}$ (where $k_\perp$ denotes the wavevectors perpendicular to $\mathbf{\Omega}$) with a non-self-similar behavior along the axis parallel to the rotation has been suggested in [45] on the basis of numerical results.

In numerical simulations, the study of rotating turbulent flows is constrained by the computational cost of properly resolving the inertial waves and the resonant triadic interactions, together with the cost of resolving the small scale fluctuations when the Reynolds number is large. Inverse cascades were shown to develop and anisotropies to appear in low resolution (32^3 and 64^3 grid points) simulations [8, 9, 27], either solving the equations of motion directly or using a subgrid model. Small aspect ratio boxes were considered in [51, 53] allowing for an increase in resolution. Simulations at higher resolution were done later in [59], studying in particular the behavior of the shell-to-shell energy transfer. Recently, simulations with large Reynolds number and small Rossby number were performed using 128^3 grids and 8th-order hyperviscosity [19], thus confirming the dominant role of resonant triads for rapid rotation at large Re, although the results also suggest that resonant wave theory can be valid only for a finite interval of time ; this has been argued by a number of authors in the general context of wave turbulence because of the non uniformity in scale of the method, as already discussed earlier. Also note that all these simulations give different results for the scaling of the energy spectrum at scales larger than the forcing scale; it was shown in [52], using a truncated model, that this can be the result of how all the relevant timescales are resolved.

In this paper, we study the effect of rotation in a turbulent flow using high resolution direct numerical simulations with up to 512^3 grid points. Simulations at this resolution were also performed recently in [45] with an injection of energy at the largest scale available; the focus was solely on the scaling of small-scale fluctuations, showing depletion of the energy cascade and reduced intermittency. Our main objective, on the other hand, is to study the statistical properties of the fluctuations in flows with moderate Rossby numbers (down to $Ro \approx 0.07$) but at Reynolds numbers large enough to observe the beginning of a turbulent scaling at scales smaller than the energy injection scale.

To this end, we use coherent forcing at intermediate scales, leaving enough room in the spectral space for an inverse cascade of energy to develop when the Rossby number is small enough. We also use the largest value of the Reynolds number allowed by our grid to observe a direct transfer of energy at small scales. After describing the simulations, we study its spectral behavior, the shell-to-shell energy transfer, scaling laws and intermittency, the geometry of the structures and finally the degree of anisotropy of the resulting flow.

II. NUMERICAL SIMULATIONS

We solve numerically the equations for an incompressible rotating fluid with constant mass density,

$$\frac{\partial \mathbf{u}}{\partial t} + \boldsymbol{\omega} \times \mathbf{u} + 2\mathbf{\Omega} \times \mathbf{u} = -\nabla \mathcal{P} + \nu \nabla^2 \mathbf{u} + \mathbf{F}, \quad (1)$$

and

$$\nabla \cdot \mathbf{u} = 0, \quad (2)$$

where $\mathbf{u}$ is the velocity field, $\boldsymbol{\omega} = \nabla \times \mathbf{u}$ is the vorticity, $\mathcal{P}$ is the total pressure (modified by the centrifugal term) divided by the mass density, and ν is the kinematic viscosity. Here, $\mathbf{F}$ is an external force that drives the turbulence, and we chose the rotation axis to be in the z direction: $\mathbf{\Omega} = \Omega \hat{z}$, with Ω the rotation frequency.

The mechanical forcing $\mathbf{F}$ is given by the Taylor-Green (TG) flow [55]

$$\begin{aligned} \mathbf{F} = F_0 \left[\sin(k_0 x) \cos(k_0 y) \cos(k_0 z) \hat{x} - \right. \\ \left. - \cos(k_0 x) \sin(k_0 y) \cos(k_0 z) \hat{y} \right], \end{aligned} \quad (3)$$

where F_0 is the forcing amplitude. The forcing injects energy directly only into the x and y components of the velocity, but with a three-dimensional dependence. However, in the absence of rotation ($\Omega = 0$), the resulting flow is fully three-dimensional even in the absence of instabilities (turbulence) because pressure gradients excite the z component of the velocity [43, 55]. The TG flow has a small spectral anisotropy with slightly more energy in the z direction (see section VI form more details), an effect that is the opposite of the tendency towards two-dimensionalization due to rotation when Ω is non-zero). The flow has no net helicity, although locally regions with strong positive and negative helicity develop. It is also worth noting that this forcing injects zero energy in the $k_z = 0$ mode, whose amplification observed in the strongly rotating cases (see below) is thus only due to a cascade process.

The TG flow is important in hydrodynamics for the insights it provides. It was originally motivated as an initial condition which, though highly symmetric, would lead to the rapid development of small spatial scales [55], and as a result proposed as a paradigm of the direct cascade of energy in turbulence. It also mimics the von Kármán flows between two counter-rotating disks used in several turbulence experiments, including experiments of rotating turbulence [50] and recent experiments to reproduce generation of magnetic fields by dynamo action [42].

TABLE I: Parameters used in the simulations. N is the linear grid resolution, k_0 the wavenumber used in the forcing, ν the kinematic viscosity, Ω the rotation rate, $t_{\max}$ the maximum number of turnover times computed; Re, Ro, and Ek are respectively the Reynolds, Rossby and Ekman numbers. Note that runs A and B_1 all start from a fluid at rest, whereas runs $B_{2,3}$ start from the steady state reached by run B_1 (see text).

Run	N	k_0	ν	Ω	$t_{\max}$	Re	Ro	Ek
A1	256	2	2×10^{-3}	0.08	45	900	4.50	5×10^{-3}
A2	256	2	2×10^{-3}	0.40	45	900	0.70	8×10^{-4}
A3	256	2	2×10^{-3}	0.80	45	900	0.35	4×10^{-4}
A4	256	2	2×10^{-3}	1.60	45	900	0.17	2×10^{-4}
A5	256	2	2×10^{-3}	3.20	150	900	0.09	1×10^{-4}
A6	256	2	2×10^{-3}	8.00	185	900	0.03	3×10^{-5}
B1	512	4	8×10^{-4}	0.40	17	1100	1.40	1×10^{-3}
B2	512	4	8×10^{-4}	1.60	25	1100	0.35	3×10^{-4}
B3	512	4	8×10^{-4}	8.00	40	1100	0.07	6×10^{-5}

Two sets of runs were done at resolutions of 256^3 (set A) and 512^3 grid points (set B). The parameters for all the runs are listed in Table I. With Taylor-Green forcing, the spherical shell in Fourier space where energy is injected has wavenumber $k_F = \sqrt{3}k_0$, or equivalently, at a scale $L_F = 2\pi/k_F$. For the runs in set A, $k_F \approx 3.5$, and for the runs in set B, $k_F \approx 6.9$; as a result, there is more room in spectral space for an inverse cascade to take place in the B runs; the B runs also have a slightly higher Reynolds number.

All the runs in set A were started from a fluid at rest. At $t = 0$, the rotation and the external forcing were switched on, until reaching a turbulent steady state, or until an inverse cascade was well developed in the case of large rotation rates. The runs in set B were done as follows. Run B1 was started from a fluid at rest and after turning on the rotation and external forcing, the run was continued to reach a turbulent steady state. Runs B2 and B3 were started from a snapshot of the velocity field from the steady state of run B1, and both runs were continued until a new steady state was reached, or an inverse cascade developed. This latter method proved useful in saving computing time, as no differences were observed when comparing the late time evolution of the runs in the two sets. In order to measure the extent of the transient regime in each case (see Sec. III), and make sure the energy transfer and other relevant quantities were measured in the developed turbulent regime. To this end, all simulations were extended for very long times; Table I gives the characteristics of the runs; note that times are expressed in units of the turn-over time $\tau_{NL} = U_{rms}/L_F \sim 1/L_F$ (see below). Finally, in all simulations, a dissipative range was properly resolved, and the time step was much smaller than all the relevant timescales.

We define the integral and Taylor scales of the flow

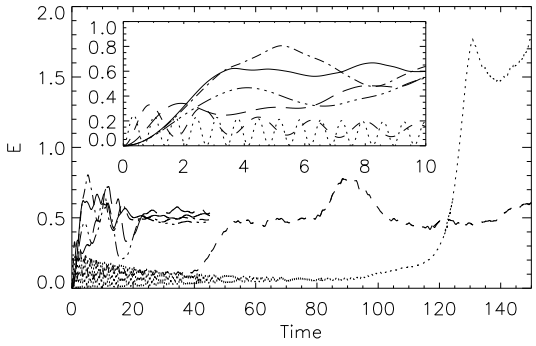

FIG. 1: Time history of the energy for set A: A1 (solid), A2 (dash-dot), A3 (dash-triple dot), A4 (long dash), A5 (dash), and A6 (dot); Rossby numbers range from 4.50 to 0.03. The inset shows a detail of the evolution at early times: at high rotation rates (runs A5 and A6), waves prevail and the energy of the system is lower than when little rotation is present. Note the transition to a high energy regime at later times as Ro decreases, because of an inverse energy cascade setting in.

respectively as

$$L = 2\pi \frac{\int E(k) k^{-1} dk}{\int E(k) dk}, \tag{4}$$

and

$$\lambda = 2\pi \left(\frac{\int E(k) dk}{\int E(k) k^2 dk} \right)^{1/2}, \tag{5}$$

where $E(k)$ is the energy spectrum. Since for large Ω an inverse cascade develops, these two scales are useful to describe the evolution of characteristic scales in the flow with time. However, to avoid a time dependence of the Reynolds and Rossby numbers (time dependent Rossby numbers based on inertial-range scales are discussed in Secs. V and VI), we define for each run the Reynolds number as

$$Re = \frac{L_F U}{\nu}, \tag{6}$$

and the Rossby number as

$$Ro = \frac{U}{2\Omega L_F}. \tag{7}$$

We also define the Ekman number as

$$Ek = \frac{Ro}{Re} = \frac{\nu}{2\Omega L_F^2}. \tag{8}$$

The turnover time at the forcing scale is then defined as $T = L_F/U$ where $U = \sqrt{\langle u^2 \rangle}$ is the r.m.s. velocity measured in the turbulent steady state, or when the inverse cascade starts. The amplitude of the forcing F_0 in the simulations is increased as Ω is increased in order to have $U \approx 1$ in all the runs.

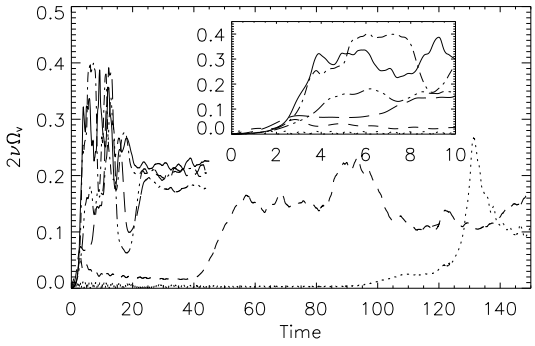

FIG. 2: Time history of the energy dissipation rate (labels as in Fig. 1); the inset again shows the evolution at early times. Note that after transients with little dissipation (and thus little turbulence), runs A3 to A6 reach approximately half the level of turbulence activity of the non rotating flows, as measured by their dissipation rate.

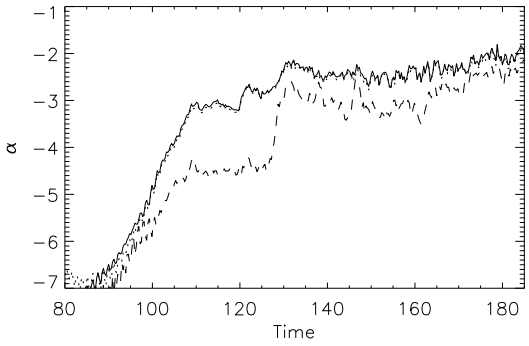

FIG. 3: Spectral index α as a function of time in run A6, in the isotropic energy spectrum $E(k)$ (solid), in the $E(k_\perp)$ spectrum (dot), and in the $E(k_\parallel)$ spectrum (dash). Note that the energy distribution, as measured by α, is dominated by the orthogonal modes.

III. TIME EVOLUTION AND SPECTRA

Figure 1 shows the time history of the energy in the runs in set A. Runs A1-A4 show a similar evolution, but runs A5 and A6 evolve differently. As the Rossby number decreases, a transient develops in which the total energy oscillates with a frequency that increases with Ω. Examining the inset, the period of oscillation of the total energy in that first phase decreases monotonically from run A3 to run A6; for the dissipation (see below), this oscillation is only clearly seen at the lowest Rossby number in run A6. The transition time between this wave-dominated regime to another regime grows as Ω increases, for sufficiently large Ω. Then, the energy increases suddenly and a fully turbulent regime finally develops, including at the lowest Rossby number. An inverse cascade of energy is observed in run A6 after $t \approx 120$. The increase in the energy observed after this time is also accompanied by a monotonous increase with time of the flow integral scale L. Even in the runs in set B, that are restarted from a pre-existing turbulent steady state, long runs are needed to reach another turbulent state after turning on the rotation. As an example, in run B3 it takes ≈ 20 turnover times for the transient to decay and for an inverse cascade of energy to develop.

The energy dissipation rate $2\nu\Omega_\nu \equiv \nu \int \omega^2 dV$ as a function of time is shown in Fig. 2. As the Rossby number decreases, the peak of the dissipation rate is reached at later times, and then it saturates. Note that during the early transient in runs A5 and A6, the dissipation is almost negligible (corresponding likely to a wave turbulence regime with substantially reduced nonlinear interactions), while in the saturated state the mean dissipation rate decreases slowly with decreasing Rossby number.

The shape of the energy spectrum evolves with time, specially after the transient as turbulence sets in, and later again as the spectrum becomes dominated by the contribution from the largest scales when the Rossby number is small enough for an inverse cascade to develop. Figure 3 shows the time evolution of the spectral index α (the exponent in the region of the spectrum with $k > k_F$ that follows a power law $\sim k^\alpha$) in run A6. Three curves are shown, which correspond respectively to the spectral index computed on the isotropic energy spectrum $E(k)$, on the perpendicular energy spectrum $E(k_\perp)$ (where $k_\perp$ denotes the wavevectors perpendicular to $\mathbf{\Omega}$), and the parallel spectrum $E(k_\parallel)$ (where $k_\parallel$ denotes the wavevectors parallel to $\mathbf{\Omega}$). Here and in the following, the isotropic energy spectrum $E(k)$ is defined by averaging in Fourier space over spherical shells, and the reduced energy spectra $E(k_\perp)$ and $E(k_\parallel)$ are defined averaging in Fourier space respectively over cylinders and over planes; a detailed definition of these averages can be found in Sec. IV, Eqs. (10-12).

Before $t \approx 80$, we cannot recognize a power law in the energy spectra. After $t \approx 80$, the spectral indices in $E(k)$ and $E(k_\perp)$ grow monotonically from a value of -7 until reaching a plateau with $\alpha \approx -3$ at $t \approx 110$. The energy spectra $E(k)$, $E(k_\perp)$, and $E(k_\parallel)$ show wide and steep power law behavior from $t \approx 80$ to $t \approx 120$. During this transient, the energy flux is almost zero, as can also be expected from the small value of the energy dissipation in run A6 before $t \approx 110$ (Fig. 2). The end of the transient at $t \approx 110$ and the plateau in α correspond respectively to the increase in the energy and in the energy dissipation rate showed in Figs. 1 and 2. The spectral index in $E(k_\parallel)$ also has a plateau with $\alpha \approx -4.5$. However, as the inverse cascade sets in and the energy piles up at the largest available scale in the system, the spectral index changes again and seem to slowly evolve towards $\alpha \approx -2$ in both $E(k)$ and $E(k_\perp)$. $E(k_\parallel)$ evolves towards a steeper spectrum with a strong peak at $k_\parallel = 0$.

Note that the inverse cascade only starts after ≈ 10 turnover times after the turbulent state is reached at $t \approx$

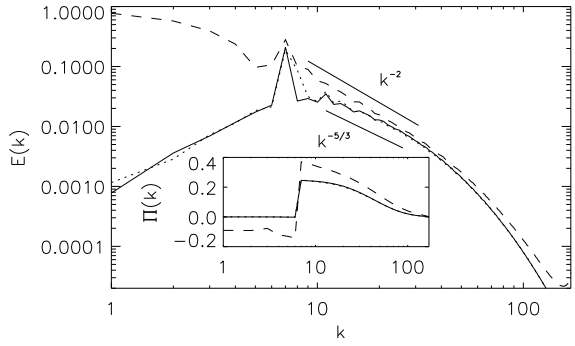

FIG. 4: Isotropic energy spectra at late times in runs B1 (solid, $t \approx 16$), B2 (dot, $t \approx 24$), and B3 (dash, $t \approx 40$) at low *Ro*. Two slopes are given as a reference. The inset shows the isotropic energy flux for the same runs. Note that B1 and B2 are almost undistinguishable, and that an inverse cascade develops only for B3.

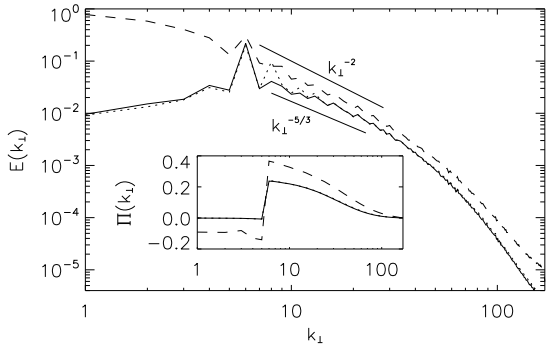

FIG. 5: $E(k_\perp)$ and $\Pi(k_\perp)$ (inset) at late times in runs B1, B2, and B3. Labels are as in Fig. 4.

110. This can be understood as follows. The energy spectrum observed before $t \approx 110$ has almost no flux. Nonlinear transfer of energy is required for the flow to become two-dimensional under the effect of rotation [16, 53, 57], and the nonlinear transfer is negligible until $t \approx 110$. Then, after a few turnover times, the flow undergoes a transition and the inverse cascade sets in.

The long transient is only observed in the runs in set A, since the runs in set B are started from a turbulent steady state. However, after the transient, the spectral evolution of the runs in set A and B is similar. Since runs in set B have more scale separation for an inverse cascade to develop when *Ro* is small enough, we focus now on this set of runs. We show in Fig. 4 the isotropic energy spectrum at late times in runs B1-B3. While runs B1 and B2 show no growth of energy at scales larger than the mechanical forcing, except for some backscattering with a $\sim k^2$ spectrum, run B3 at late times is dominated by the energy in the $k = 1$ shell. At scales smaller than the forcing scale, the spectrum of run B3 is steeper than that

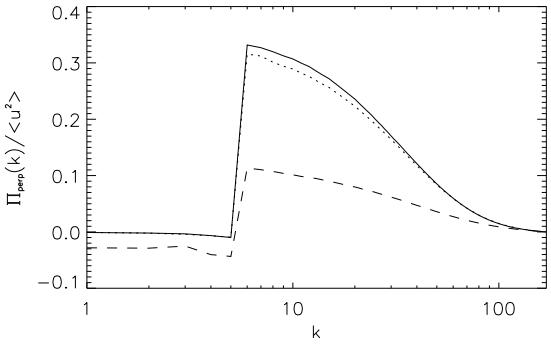

FIG. 6: $\Pi(k_\perp)/\langle u^2 \rangle$ at late times in runs B1, B2, and B3. Labels are as in Fig. 4.

of runs B1 and B2, and compatible with a $\sim k^{-2}$ scaling. The inset in Fig. 4 shows the isotropic energy flux in the same runs. Note that in run B3, the flux at scales larger than the forcing scale is negative and approximately constant, indicating the development of an inverse cascade of energy for small *Ro*, although at a lower intensity than the direct cascade. At smaller scales, the energy flux is positive. We thus conclude that in rotating flows, both the direct and inverse energy cascades can cohabit.

The energy spectrum $E(k_\perp)$ is shown in Fig. 5, together with the energy flux $\Pi(k_\perp)$. The spectrum and flux are similar to the isotropic ones (indicating that most of the energy is in these modes), and $\Pi(k_\perp)$ confirms the development of an inverse cascade of energy in $k_\perp$ at scales larger than the forcing scale in run B3, and a direct cascade at smaller scales with a $\sim k_\perp^{-2}$ scaling. Figure 6 shows the energy flux $\Pi(k_\perp)$ normalized by the r.m.s. velocity in each run. Note that the increase of the flux observed in the inset of Fig. 5 is only due to the increase in the energy of the system as the inverse cascade piles up energy at the largest available scale. As Fig. 6 indicates, the actual transfer of energy is slowed down by the rotation, and run B3 shows a smaller normalized flux than the other two runs at scales smaller than the forcing scale.

On the other hand, there is no clear scaling in the small scales in $E(k_\parallel)$, nor an inverse cascade at large scales (see Figure 7). The $E(k_\parallel)$ spectrum in run B3 is steeper than the $E(k_\perp)$ spectrum, consistent with the results shown in Fig. 3 for run A6 at late times. Slopes $\sim k^{-5/3}$ and $\sim k^{-2}$ are shown in Fig. 7 only as a reference.

Before proceeding to the computation of the transfer function and other high-order statistics, it is worth pointing out that the long transient observed in runs in set A, as well as a shorter transient observed at early times in the runs in set B, make computation of long runs crucial for the following analysis. In run A6, which was started from a fluid initially at rest, the inverse cascade only starts after $t \approx 120$. But even in run B3, which was started from a previous turbulent steady state, a transient with oscillations in the energy and the enstrophy

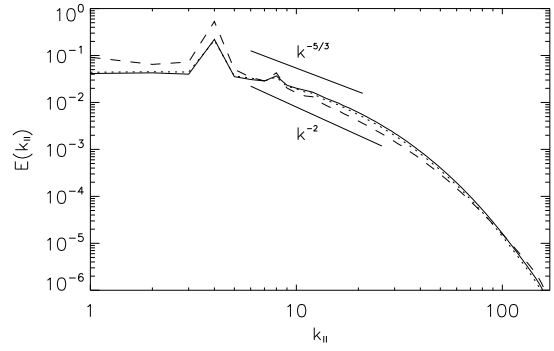

FIG. 7: $E(k_\parallel)$ at late times in runs B1, B2, and B3. Labels are as in Fig. 4.

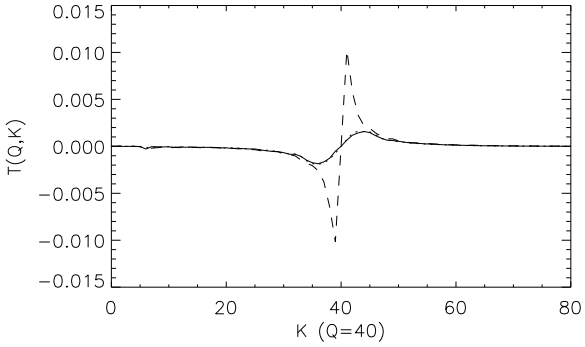

FIG. 8: Shell-to-shell transfer function $T(Q, K)$ at $Q = 40$ for runs B1 (solid), B2 (dot), and B3 (dash) at late times.

is observed at early times, which are damped only after ≈ 10 turnover times.

IV. ENERGY TRANSFER

In this section we study the scale interactions and energy transfer in rotating turbulent flows. A study of the energy transfer in this context, albeit at lower resolution and earlier times, was done before by [59]. We will focus on runs B1, B2, and B3, that have enough scale separation for direct and inverse cascades to develop when *Ro* is small enough. Similar results were obtained in the analysis of the runs in set A.

To investigate the transfer of energy among different scales we consider the shell filter decomposition of the velocity field,

$$\mathbf{u}(\mathbf{x}) = \sum_K \tilde{\mathbf{u}}_K(\mathbf{x}), \tag{9}$$

where K denotes a foliation of Fourier space in shells, that for our purposes can be taken as spheres [2, 3, 37, 38]

$$\mathbf{u}_K(\mathbf{x}) = \sum_{K\le|\mathbf{k}|\le K+1} \tilde{\mathbf{u}}_\mathbf{k} e^{i\mathbf{k}\cdot\mathbf{x}}, \tag{10}$$

cylinders [1]

$$\mathbf{u}_{K_\perp}(\mathbf{x}) = \sum_{K\le|\mathbf{k}_\perp|\le K+1} \tilde{\mathbf{u}}_\mathbf{k} e^{i\mathbf{k}\cdot\mathbf{x}}, \tag{11}$$

or planes [1]

$$\mathbf{u}_{K_\parallel}(\mathbf{x}) = \sum_{K\le|\mathbf{k}_\parallel|\le K+1} \tilde{\mathbf{u}}_\mathbf{k} e^{i\mathbf{k}\cdot\mathbf{x}}. \tag{12}$$

Then, we can define the shell-to-shell transfer between these shells as

$$T(Q, K) = -\int \mathbf{u_K}(\mathbf{u}\cdot\nabla)\mathbf{u_Q}\, d\mathbf{x}^3. \tag{13}$$

This function expresses the transfer rate of energy lying in the shell Q to energy lying in the shell K. It satisfies the symmetry property $T(Q, K) = -T(K, Q)$ [3], and the numbers labeling the shells Q and K can correspond to any of the foliations of Fourier space listed above [1]. In particular, we will study the cases $T(Q, K)$, $T(Q_\perp, K_\perp)$, and $T(Q_\parallel, K_\parallel)$. The energy fluxes discussed in the previous section can be reobtained in terms of the shell-to-shell transfer function as

$$\Pi(k) = -\sum_{K=0}^{k}\sum_{Q} T(Q, K), \tag{14}$$

where again the wavenumbers k, K, and Q can correspond to different foliations of Fourier space depending on the subindex.

Note that for the definition of the shells a linear binning is used. Alternatively, the shells can be defined by a logarithmic binning of spectral space with intervals $(\gamma^n K_0, \gamma^{n+1} K_0]$ for some positive $\gamma > 1$ and for integer n. However, logarithmic binning cannot distinguish transfer between linearly spaced neighbor shells (from the shell K to the shell $K+1$) from the transfer between logarithmic neighbor shells (from K to γK). If the cascade is the result of interactions with the large-scale flow (e.g., with modes with wavenumber k_F associated to the external forcing), the energy in a shell K will be transferred to the shell $K + k_F$. Logarithmic binning does not distinguish this transfer from the transfer due to local triadic interactions that transfer the energy from K to γK. For this reason we use linear binning, but we note that care needs to be taken when using the word "scale" that implies in general a logarithmic division of the spectral space. The transfer among logarithmic shells can be reconstructed at any time later by summing over the linearly spaced shells.

Figure 8 shows the shell-to-shell transfer $T(Q, K)$ at $K = 40$ for runs B1, B2, and B3 at late times. The negative peak to the left indicates energy is transferred from

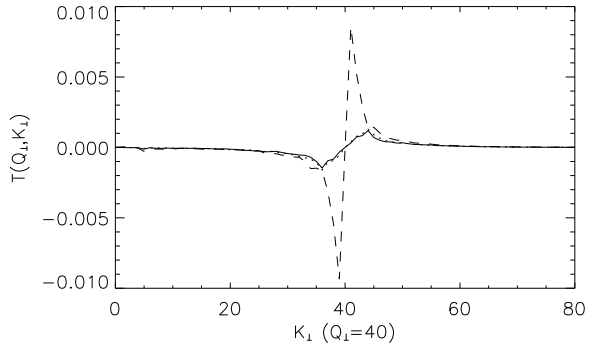

FIG. 9: Shell-to-shell transfer function $T(Q_\perp, K_\perp)$ at $Q_\perp = 40$ for runs B1, B2, and B3. Labels are as in Fig. 8.

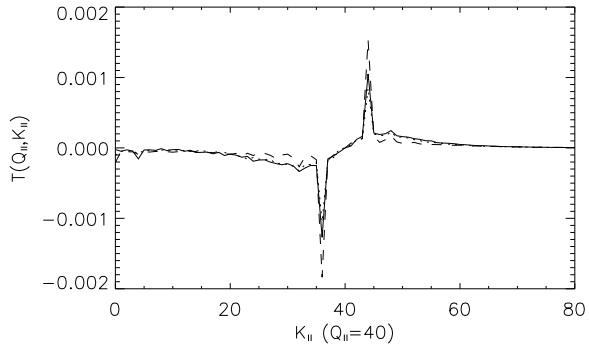

FIG. 10: Shell-to-shell transfer function $T(Q_\parallel, K_\parallel)$ at $Q_\parallel = 40$ for runs B1, B2, and B3. Labels are as in Fig. 8. Notice these transfers are roughly 5 times weaker than in the $\perp$ case.

these K-shells to the shell $Q = 40$, while the positive peak to the right indicates energy goes from the $Q = 40$ shell to those K-shells. In runs B1 and B2 the shell-to-shell transfer peaks at $|Q-K| \approx k_F$. This was observed before in simulations of homogeneous turbulence [2, 21, 22, 38], and indicates that the energy transfer is local (the energy goes from a shell Q to a nearby shell K, although the step in the energy cascade is independent of that scale and related to the forcing scale). In the context of the present study, it is worth mentioning that this is not a peculiarity of the TG forcing, and this transfer in non-rotating turbulence has been observed for other forcing functions, including isotropic delta-correlated in time forcing [22, 38]. It is the result of individually strong triadic interaction involving the energy containing scale. As more triads are summed in order to obtain the shell-to-shell transfer and the energy flux, the functions become more local; at the Reynolds number studied here, it can be shown that $\approx 60\%$ of the energy flux in the non-rotating case is due to local interactions [41].

The shell-to-shell transfer in run B3 is markedly different and strongly peaks at $|Q-K| \approx 1$. The same effect is observed in $T(Q_\perp, K_\perp)$ shown in Fig. 9. This indicates that at late times in run B3, the direct transfer of energy at small scales is mediated by interactions with the largest scale in the system, the energy containing eddies with $k_\perp \approx 1$ (see Fig. 5). As a result, the timescale associated with the direct cascade of energy in $k_\perp$ increases (and its flux reduces, see Fig. 6), since the energy is transferred in smaller steps in Fourier space than in the case of the B1 and B2 runs.

The shell-to-shell transfer $T(Q_\parallel, K_\parallel)$ at $Q_\parallel = 40$ for the same runs is shown in Fig. 10. The dependence with the Rossby number of this transfer function is less drastic. In all runs, the transfer function $T(Q_\parallel, K_\parallel)$ peaks at $|Q_\parallel - K_\parallel| \approx k_F$. Although, there is considerable amount of energy in the shell $k_\parallel = 0$, the modes in this shell (that correspond to a pure 2-D flow) do not cascade the energy in the $k_\parallel$ axis since they are unable to stretch eddies in the z-direction. As a result, the cascade in this direction is only due to modes with $k_\parallel > 0$ and the modes with $k_\parallel = k_F$ dominate. Note also that there is a drop in the amplitude of the transfer in run B3 for all shells except the ones satisfying $|Q_\parallel - K_\parallel| = k_F$. As a result, for small Rossby number the transfer of energy between shells with $Q_\parallel$ and $K_\parallel$ is quenched except for the direct interactions with the external forcing. Most of the interactions responsible for the transfer of energy to small scales between different $k_\parallel$ shells at small *Ro* are then interactions with the forcing. This is consistent with previous results showing that rotation reduces the turbulent energy transfer along the parallel direction.

Figure 11 shows the transfer functions $T(Q_\perp, K_\perp)$ and $T(Q_\parallel, K_\parallel)$ in runs B1 and B3 for all values of K and Q up to 40. In all cases, the white and black bands near $K \approx k_F$ and $Q \approx k_F$ indicate a small amount of energy injected by the external forcing that is directly transferred to all wavenumbers up to ≈ 30. For K and Q larger than k_F, the figures confirm the results of the direct cascade of energy presented in Figs. 9 and 10. For wavevectors perpendicular to $\mathbf{\Omega}$, as the Rossby number is decreased, the peaks in $T(Q_\perp, K_\perp)$ move closer to the diagonal $K_\perp = Q_\perp$ [Figs. 11(a) and (b)], indicating the direct cascade in the perpendicular direction takes place in smaller k-steps given by the largest scale of the system. For all wavevectors, the energy in the parallel direction [see $T(Q_\parallel, K_\parallel)$ in Figs. 11(c) and (d)] is transferred to smaller scales, and the cascade step does not depend on the Rossby number. However, all transfer except the transfer with $|Q_\parallel - K_\parallel| = k_F$ is strongly quenched in run B3.

The development of a non-local inverse transfer can be observed in Fig. 11(b) for $K_\perp < k_f$ and $Q_\perp < k_f$. The transfer is inverse, since below the diagonal $Q_\perp = K_\perp$ regions with negative (dark gray and black) $T(Q_\perp, K_\perp)$ can be observed. This means that energy is taken from e.g., $K_\perp = 20$ and transferred to shells with $Q_\perp < k_F$. The transfer is also non-local, since this inverse transference takes place between disparate scales. The non-local transfer of energy in rotating turbulence shares similarities with the inverse cascade of magnetic helicity in

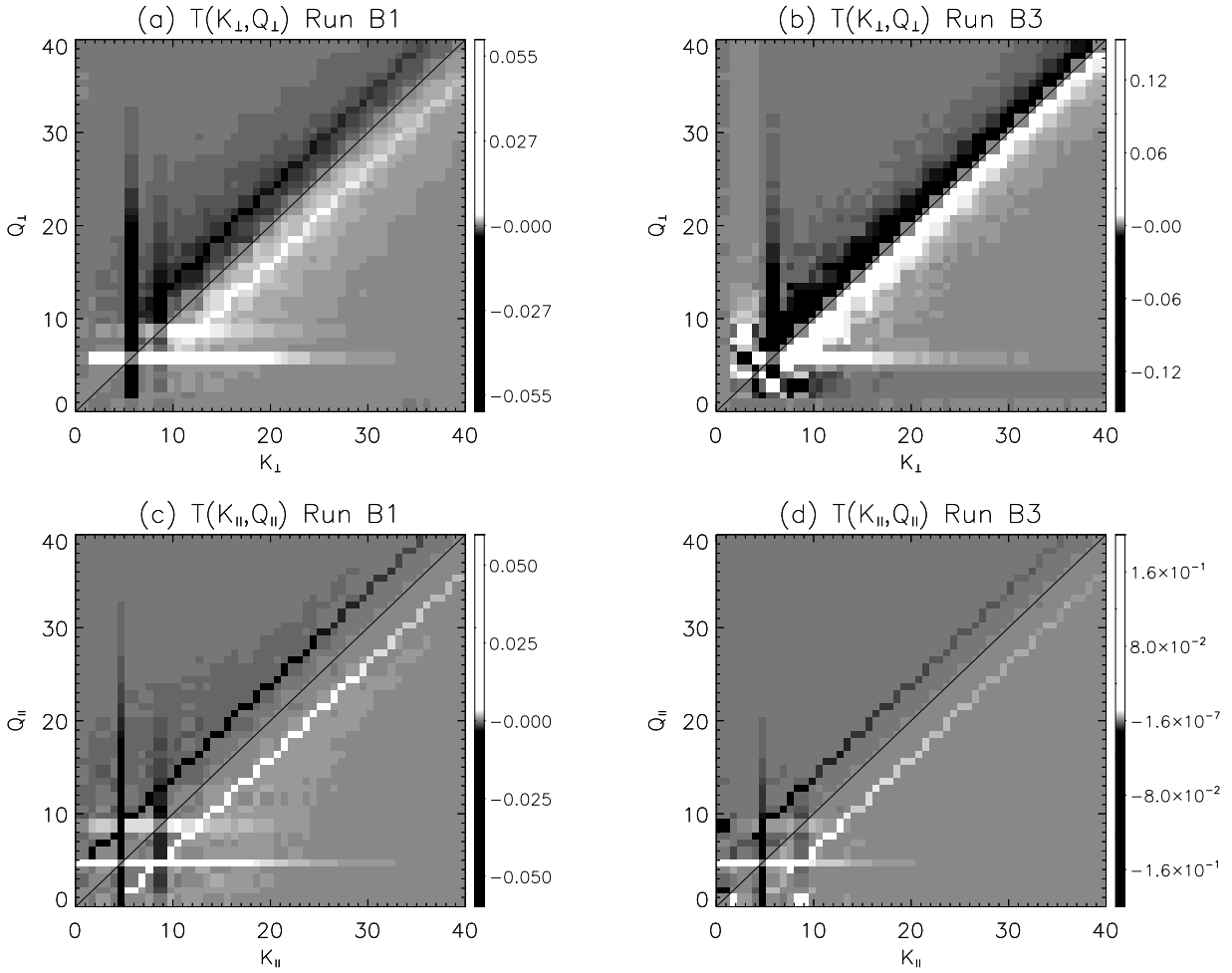

FIG. 11: Shell-to-shell energy transfer functions $T(Q_\perp, K_\perp)$ (a,b) and $T(Q_\parallel, K_\parallel)$ (c,d) at late times in runs B1 (a,c) and B3 (b,d). Notice the quenching of the transfer in case (d), except for the interactions with the forcing scale.

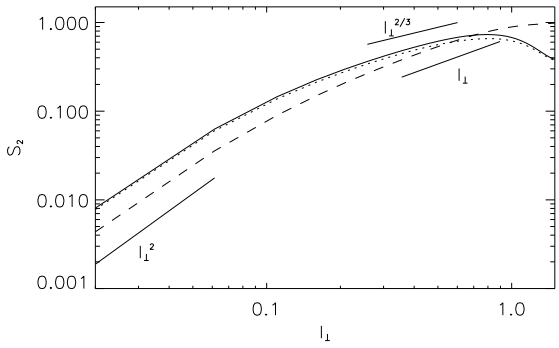

FIG. 12: Second order longitudinal structure function $S_2(\ell_\perp)$ (where $\ell_\perp$ denotes increments were taken in the direction perpendicular to $\mathbf{\Omega}$) for runs B1 (solid), B2 (dot), and B3 (dash).

magnetohydrodynamics (MHD) [4, 5]. Near the diagonal $Q_\perp = K_\perp$ the transfer is more complex. The inverse transfer superposes with a (smaller in net amplitude) direct local transfer (dark spots below and near the diagonal, and light spots above and near it, for $K_\perp$ and $Q_\perp$ smaller than k_F). This small direct transfer of energy at large scales is the result of a reflection of energy at $K = 1$, and was also observed in studies of the inverse cascade of magnetic helicity in MHD [4]. The reflection of energy in Fourier space when it reaches the largest scale in the box suggests that the late time evolution can be dependent on the boundary conditions, a property that was already observed in simulations of two dimensional turbulence [6, 11, 14, 33, 34]. In our case, the simulations do not contain a large-scale dissipation mechanism (such as a hypo-viscosity), and therefore energy piles up at the largest available scale until its growth is stopped by the (small-scale) dissipation.

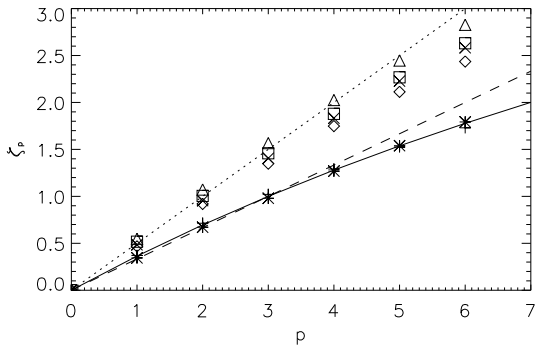

FIG. 13: Scaling exponents ζ_p for the steady state of runs B1 (+), B2 (∗), and for run B3 at different times: $t \approx 20$ (◊), $t \approx 25$ (×), $t \approx 30$ (□), and $t \approx 40$ (△). The solid line corresponds to the scaling exponents given by the She-Lévêque model [48], the dash line is the Kolmogorov prediction $\zeta_p = p/3$, and the dotted line is $\zeta_p = p/2$. Note that in run B_3, as time evolves, the exponents approach the $p/2$ scaling (see text).

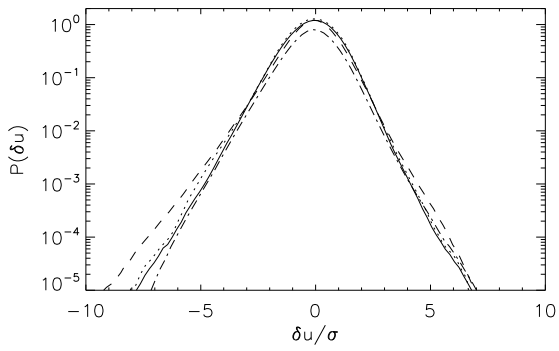

FIG. 14: Pdf of the longitudinal velocity increments ($\ell_\perp = 3\eta$) for run B3 at different times: $t \approx 20$ (solid), $t \approx 25$ (dot), $t \approx 30$ (dash), and $t \approx 40$ (dash-dot); η is the Kolmogorov dissipative length and σ is the root mean square deviation of the velocity increments.

TABLE II: Characteristic scales and dimensionless numbers of the runs in set B. t is the time, $L_\parallel$ and $L_\perp$ are the integral scales using respectively the $E(k_\parallel)$ and $E(k_\perp)$ spectra, λ is the isotropic Taylor scale, Ro_λ is the micro-Rossby number based on the Taylor scale, and $\mu = 2\zeta_3 - \zeta_6$.

Run	t	$L_\parallel$	$L_\perp$	λ	Ro_λ	μ
B1	16	1.5	0.9	0.29	3.70	0.23 ± 0.01
B2	24	1.6	0.9	0.31	0.91	0.24 ± 0.01
B3	20	2.6	1.2	0.50	0.12	0.19 ± 0.02
B3	25	2.4	1.5	0.55	0.11	0.26 ± 0.02
B3	30	2.1	1.7	0.59	0.12	0.26 ± 0.05
B3	40	1.9	2.8	0.53	0.33	0.24 ± 0.02

V. SCALING LAWS AND INTERMITTENCY

In this section, we consider the anisotropic inertial range scaling of the runs in Table I as described by the longitudinal velocity increments in the direction perpendicular to rotation,

$$\delta u(\mathbf{x}, \ell_\perp) = \hat{\mathbf{r}} \cdot [\mathbf{u}(\mathbf{x} + \ell\hat{\mathbf{r}}) - \mathbf{u}(\mathbf{x})] \,, \tag{15}$$

where $\hat{\mathbf{r}}$ is a unit vector perpendicular to $\mathbf{\Omega}$. The longitudinal structure functions $S_p(\ell_\perp)$ (with displacements along $\ell_\perp$) can then be defined as

$$S_p(\ell_\perp) = \langle \delta u(\mathbf{x}, \ell_\perp)^p \rangle \,, \tag{16}$$

where the brackets denote spatial averaging. If the flow is self-similar, we expect $S_p(\ell_\perp) \sim {\ell_\perp}^{\zeta_p}$, where ζ_p are the scaling exponents. In isotropic and homogeneous hydrodynamic turbulence, the Kármán-Howarth theorem implies $S_3(\ell) \sim \ell$, and the Kolmogorov energy spectrum follows from the assumption $S_p(\ell) \sim \ell^{p/3}$ [24]. In practice, the spontaneous development of strong gradients in the small scales of a turbulent flow gives rise to corrections to this scaling, a phenomenon referred to as intermittency.

From dimensional analysis, if the energy spectrum at small scales in rotating turbulence is $E \sim k_\perp^{-2}$, we expect $S_2 \sim \ell_\perp$. Figure 12 shows the second order structure function for runs B1, B2, and B3 at late times outside the wave regime when the turbulence has developed. At small scales for all runs, $S_2 \sim \ell_\perp^2$, consistent with a smooth field in the dissipative range. At large scales, S_2 is larger for run B3 than for runs B1 and B2, a signature of the inverse cascade of energy and of the development of large scale structures in the flow. The scaling of runs B1 and B2 at intermediate scales is compatible with the Kolmogorov spectrum, while the scaling in run B3 is consistent with the $\sim k_\perp^{-2}$ energy spectrum. Note that such a scaling can be understood as a slow-down in the energy transfer rate because of interactions between waves and eddies (see e.g., [40, 45, 61]); such a slow-down is consistent with the results of the transfer function presented in the previous section. Considering that the energy flux in the inertial range ϵ is slowed down by waves (see e.g., [28, 30] for the MHD case)

$$\epsilon \sim \delta u_{\ell_\perp}^2 \tau_\Omega / \tau_{\ell_\perp}^2 \,, \tag{17}$$

where $\tau_\Omega \sim 1/\Omega$, and $\tau_{\ell_\perp} \sim \ell_\perp / \delta u_{\ell_\perp}$ is the turnover time of eddies in the plane perpendicular to $\mathbf{\Omega}$; the scaling

$$\delta u_{\ell_\perp}^2 \sim \ell_\perp \tag{18}$$

follows.

Figure 13 shows the scaling exponents ζ_p up to order 6 computed in runs B1, B2, and B3. The scaling exponents are defined as the exponents in

$$S_p(\ell_\perp) \sim \ell_\perp^{\zeta_p} \tag{19}$$

in the inertial range associated to the direct cascade of energy (i.e., for $\ell_\perp < L_F$). Runs B1 and B2 behave as non-rotating turbulence, with Kolmogorov scaling ($\zeta_2 \approx 2/3$)

and intermittency corrections (the prediction $\zeta_p = p/3$ of Kolmogorov, and the model of intermittency in homogeneous and isotropic turbulence of She and Lévêque [48] are shown in Fig. 13 as a reference). However, run B3 has a distinct behavior, with $\zeta_2 \approx 1$. As time evolves in this run, and the energy piles up at $k_\perp \approx 1$, the second order scaling exponent slowly converges to this value. Low order moments follow the curve $\zeta_p = p/2$, but high order moments deviate from the straight line.

Similar results were found in an experimental study of a turbulent flow between two co-rotating disks [50] (see also [47]). The resulting experimental flow shares similarities with the TG flow studied here. In the experiment, a transition from isotropic and homogeneous turbulence scaling to a $\zeta_p = p/2$ scaling was observed as measurements were made closer to the intense large-scale vortex formed in the gap between the two disks.

The level of intermittency in the flow in all these runs can be measured in terms of $\mu = 2\zeta_3 - \zeta_6$. This quantity, together with the integral scales of the flow (based on the parallel and perpendicular energy spectra), the Taylor scale, and the micro-Rossby number (based on the Taylor scale of the flow),

$$Ro_\lambda = \frac{U}{2\Omega\lambda}, \tag{20}$$

are given in Table II for the runs in set B at different times. The value of the micro-Rossby number plays a central role in the determination of the velocity derivative skewness and the inhibition of the energy cascade in rotating turbulence, as discussed in Ref. [16]. In addition, its value is also important in the development of anisotropies through non-linear interactions, as is discussed in more detail in the next section.

It can be seen that at late times run B3 evolves towards an anisotropic state in the large scales, with $L_\perp/L_\parallel \approx 1.5$ (see Sec. VI for more details). However, at small scales the flow seems more isotropic and at late times ($t \approx 40$) in this run $\lambda_\perp/\lambda_\parallel \approx 0.8$. The micro-Rossby number in runs B1, B2, and B3 takes different values, in the range 0.11–3.7. However, the value of μ is, within error bars, approximately the same for all the runs. As a result, the intermittency in the direct cascade of energy in a rotating flow seems to be independent of the Rossby number Ro and of the micro-Rossby number Ro_λ (in the range of Rossby numbers studied).

Finally, Figure 14 shows the time evolution of the probability density function (pdf) of the longitudinal velocity increments in run B3. Increments in the direction perpendicular to $\mathbf{\Omega}$ were computed, and the increment was taken equal to three times the Kolmogorov dissipation scale η in each run. The velocity increments in each run were normalized by their corresponding root mean square deviation σ. In agreement with the level of intermittency observed in the scaling exponents, the pdfs show exponential tails indicating a larger than Gaussian probability of large gradients to occur in the small scales. The amplitude of the tails of the pdfs as a function of $\delta u/\sigma$ does not change significantly with time. Moreover, the root mean square deviation σ of the velocity increments δu increases with time. So if the pdfs are plotted versus δu (instead of versus $\delta u/\sigma$), the pdfs actually become wider at later times. This effect can be understood considering that once the inverse cascade of energy sets in, the total energy in the flow as a function of time increases.

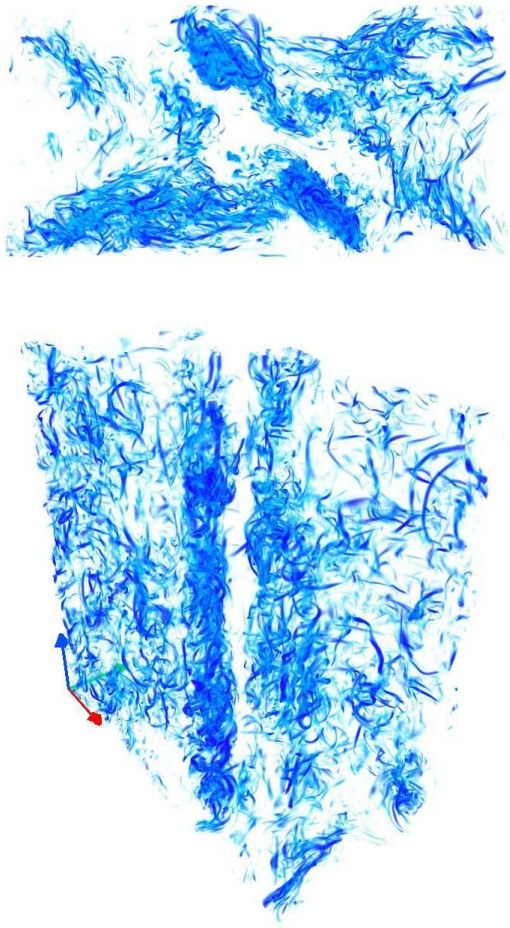

FIG. 15: (Color online) Three dimensional rendering of the vorticity intensity in a subvolume of $256 \times 512 \times 512$ grid points for run B2. The top view shows the subvolume in the direction of the axis of rotation; in the bottom view, the red and blue arrows indicate respectively the x and z axis. Note the large-scale columns made up of smaller-scale intense vortices typical of three-dimensional turbulence.

VI. STRUCTURES AND ANISOTROPY

The intermittency reported in the previous section in the scaling exponents and the pdfs of velocity increments indicates that even after the inverse cascade sets in, the flow develops strong velocity gradients in the small scales. In this section, we present visualizations of the flow and consider the structures that emerge.

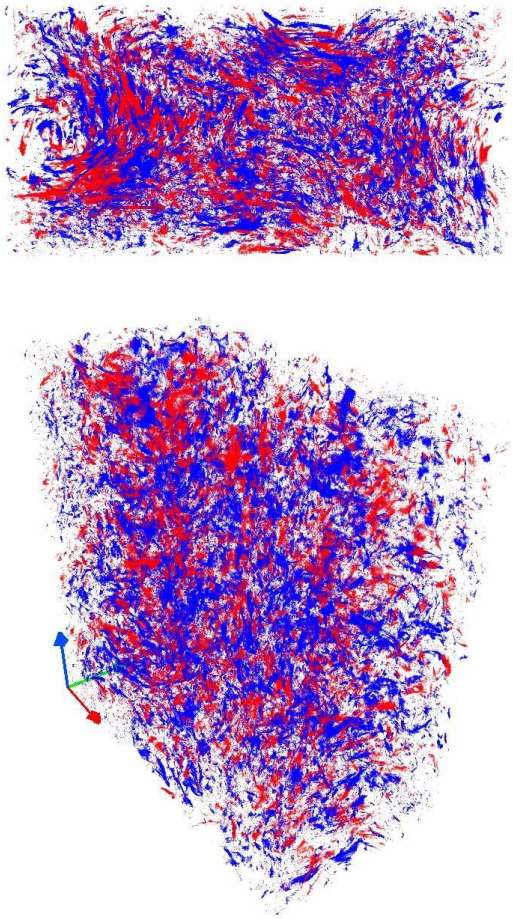

FIG. 16: (Color online) Rendering of relative helicity in the same subvolume as in Fig. 15 and with the same viewpoints. Blue corresponds to positive helicity, and red to regions with negative helicity. Only regions with $|\boldsymbol{\omega}\cdot\mathbf{u}|/(|\boldsymbol{\omega}||\mathbf{u}|) > 0.95$ are shown, i.e. for strong alignment between the velocity and vorticity, which appears ubiquitous and not confined to strong vorticity regions as in the non rotating case.

Figure 15 shows a three dimensional rendering of the vorticity intensity in half of the computational domain ($256\times512\times512$ grid points) at late times. The top view corresponds to the subvolume in the direction of the axis of rotation. Only regions with strong vorticity are shown. Note that the flow is anisotropic and quasi-2D, as it is clear from the top view. In the bottom view, the development in the flow of large scale column-like structures can be seen. However, the columns display small scale structures with thin vortex filaments. These filaments seem to be ordered according to the large scale pattern. The presence of regions with strong vorticity even when the Rossby number is small enough for the inverse cascade of energy to develop can be expected from the results shown in Figs. 13 and 14, linked to the intermittency of the flow.

The development of anisotropies in the runs with small Rossby number is apparent from Fig. 15. Table III gives a list of different measures of anisotropy commonly used in the literature, for all runs at different times. According to [16, 29], anisotropies develop in rotating flows through non-linear interactions when the Rossby number $Ro < 1$ and when the micro-Rossby number $Ro_\omega > 1$. The micro-Rossby number Ro_ω is the ratio of r.m.s. vorticity to background vorticity (rotation),

TABLE III: Different measures of anisotropy in all runs at different times. t is the time, Ro_ω is the micro-Rossby number based on the r.m.s. vorticity, $L_\perp/L_\parallel$ is the ratio of perpendicular to parallel integral scales, $\tan^2\theta$ is the square tangent of the Shebalin angle, and $E(k_\parallel=0)/E$ is the ratio of energy in all modes with $k_\parallel=0$ to the total energy.

Run	t	Ro_ω	$L_\perp/L_\parallel$	$\tan^2\theta$	$E(k_\parallel=0)/E$
A1	45	65.2	0.7	1.74	0.05
A2	45	12.7	0.7	1.78	0.07
A3	45	5.89	0.7	1.98	0.13
A4	45	3.18	0.6	2.55	0.19
A5	150	1.23	0.5	4.01	0.23
A6	110	0.22	0.4	12.3	0.15
A6	150	0.48	1.5	7.65	0.82
A6	185	1.12	1.9	3.80	0.88
B1	16	22.4	0.6	1.77	0.03
B2	24	5.61	0.6	2.04	0.11
B3	20	0.77	0.5	6.22	0.36
B3	25	0.67	0.6	6.58	0.55
B3	30	0.76	0.8	5.87	0.62
B3	40	1.35	1.5	3.82	0.66

$$Ro_\omega = \frac{\omega}{2\Omega}, \tag{21}$$

and scales as Ro_λ except for prefactors. If the macro-Rossby number Ro is too large, no inverse cascade is observed in the simulations. If the micro-Rossby number is too small, non-linear interactions are completely damped and no transition develops. It is worth noting that the actual values for the transition to occur can depend on the particular flow studied.

The development of anisotropies in rotating turbulence has been quantified in [9, 15, 16] using the parallel and perpendicular integral scales. The ratio of these two length scales is given in Table III. For $Ro \lesssim 0.35$, $L_\perp/L_\parallel \approx 0.7$ (runs A1-A3, B1, and B2); in the absence of rotation the flow under TG forcing develops a slightly larger integral scale in the z direction. However, in runs A4-A6 and B3, the ratio $L_\perp/L_\parallel$ increases and becomes larger than 1 as Ro is decreased. In runs A6 and B3, this ratio is observed first to decrease (just before the inverse cascade starts) to finally increase monotonically, reaching $L_\perp/L_\parallel \approx 1.9$ in run A6 at $t \approx 185$.

The integral scale ratio measures anisotropy in the energy containing scale. To quantify small-scale anisotropy, the so-called Shebalin angles were introduced in MHD

turbulence [36, 49],

$$\tan^2(\theta) = 2 \lim_{\ell \to 0} \frac{S_2(\ell_\perp)}{S_2(\ell_\parallel)} = 2 \frac{\sum_{k_\perp} k_\perp^2 E(k_\perp)}{\sum_{k_\parallel} k_\parallel^2 E(k_\parallel)}, \qquad (22)$$

where $\ell_\parallel$ denotes displacements along $\mathbf{\Omega}$. The angle θ measures the spectral anisotropy level, and the case $\tan^2(\theta) = 2$ corresponds to an isotropic flow. Values of $\tan^2(\theta)$ for all runs are listed in Table III. Runs A1 and B1 have $\tan^2(\theta) \approx 1.7$, a value close to isotropy and with a small anisotropy in the z direction. As the Rossby number is decreased, this tendency is reverted and $\tan^2(\theta)$ becomes larger than 2. For runs A6 and B3 the value of $\tan^2(\theta)$ is given for different times. As time evolves in these runs, the anisotropy is maximum just before the inverse cascade starts, and then $\tan^2(\theta)$ decreases slowly to saturate near ≈ 3.8.

The spectral anisotropy has also been studied through the axisymmetric energy spectrum $e(k_\parallel, k_\perp)$ (as well as other second order quantities; see e.g. [15, 16, 44, 58]). For a two dimensional flow,

$$e(k_\parallel, k_\perp) = \frac{E(k_\perp)}{2\pi k_\perp} \delta(k_\parallel). \qquad (23)$$

In rotating turbulence, a pure two-dimensional state is never reached [10]; however, a strong anisotropy develops with a steeper spectrum in the parallel direction [10, 25, 32] consistent with an integrable singularity at $k_\parallel = 0$. As an indication of this tendency, in Table III we give the ratio of energy in all modes with $k_\parallel = 0$ to the total energy $E(k_\parallel = 0)/E$; in the purely two-dimensional case this ratio is equal to one. Runs A1 and B1 have small $E(k_\parallel = 0)/E$, and the ratio increases as Ro is decreased, reaching $E(k_\parallel = 0)/E \approx 0.88$ at late times in run A6 ($Ro \approx 0.03$) and $E(k_\parallel = 0)/E \approx 0.66$ in run B3 ($Ro \approx 0.07$).

As the energy, the helicity is conserved in ideal rotating flows. However, the distribution of helicity seems to be more isotropic and homogeneous than the other quantities studied. As an example, the local relative helicity $\boldsymbol{\omega} \cdot \mathbf{u}/(|\boldsymbol{\omega}||\mathbf{u}|)$ is shown in Fig. 16, for the same subvolume as in Fig. 15. Unlike in isotropic and homogeneous turbulence, regions of strong vorticity are not correlated with regions of strong relative helicity. This is because while in isotropic and homogeneous turbulence quenching of nonlinear interactions occurs through alignment of velocity and vorticity, in rotating turbulence it results from phase-mixing and it is not necessarily linked to regions of strong helicity. The net helicity over the entire box averages to zero, and local regions with positive and negative helicity fluctuations, although ubiquitously strong, show a more isotropic and homogeneous distribution than the vorticity and velocity intensities (see e.g., Fig. 15). The study of the reasons for this behavior are left for a future work.

VII. CONCLUSIONS

In this work, we presented results of the study of the turbulent scaling laws and energy transfer in direct numerical simulations of rotating flows in periodic domains. Spatial resolutions of 256^3 (set A) and of 512^3 grid points (set B) were used, while moderate Rossby numbers (down to $Ro \approx 0.07$) and large Reynolds numbers (up to $Re \approx 1100$) were considered, with enough scale separation to observe both a direct and an inverse cascade of energy when the rotation was strong enough. Runs in set A were started from a fluid at rest, while runs in set B were restarted from a previous state of homogeneous turbulence. In the former case, for $Ro \approx 0.1$, a long transient was found in which the energy dissipation is small, as well as the energy flux to smaller scales. During this transient, the energy spectrum has a wide but steep spectrum, and its slope monotonously increases as a function of time. After turbulence sets in and the inverse cascade of energy develops, the energy spectrum evolves towards a $E \sim k_\perp^{-2}$ scaling at scales smaller than the forcing scale. This late time evolution is observed in both sets of runs.

At late times, the energy flux in runs A5, A6, and B3 corresponding to strong rotation indicates an inverse cascade of energy in $k_\perp$ at scales larger than the forcing scale, together with a direct cascade of energy at smaller scales. The net flux to small scales decreases as the Rossby number decreases, while the amplitude of the flux to large scales increases. No inverse cascade is observed in $k_\parallel$. This is consistent with the explanation of the observed tendency towards two-dimensionalization through resonant interactions [15, 57] and not through an inverse cascade in $k_\parallel$. These cascades were confirmed by the study of the shell-to-shell energy transfer. The direct transfer of energy at scales smaller than the forcing is local, although in the runs with small Rossby number the transfer in $k_\perp$ is significantly slowed down. In this direction, the energy is transferred between shells $K_\perp$ and $Q_\perp$ with small steps given by $|Q_\perp - K_\perp| \approx 1$. As a result, the direct transfer of energy in $k_\perp$ at small scales is mediated by interactions with the largest scale in the system, the energy containing eddies with $k_\perp \approx 1$. The timescale associated to the direct cascade in $k_\perp$ then increases, and its flux reduces. In $k_\parallel$ the transfer is direct at all scales, and a larger component than in the case of non-rotating turbulence is due to interactions with the forcing scale. These results are in good agreement with phenomenological derivations of the energy spectrum in rotating turbulence that consider a slow down in the energy transfer rate because of interactions between waves and eddies [45, 61]. The non-local interactions also lead to the development of anisotropies in the flow [15, 57].

The inverse cascade of energy that develops at scales larger than the forcing scale, in runs A5, A6, and B3 is non-local, in the sense that the transfer of energy associated to this cascade takes place between disparate shells in Fourier space. At late times, the inverse trans-

fer superposes with a (smaller in amplitude) direct local transfer of energy.

This small direct transfer of energy at large scales is the result of a reflection at $k_\perp = 1$, when the peak of energy reaches the largest scale in the box. Consequently, the late time evolution of simulations of rotating turbulence may depend on the boundary conditions used, a property already observed in simulations of non-rotating two dimensional turbulence [6, 11, 14, 33, 34], and on the use or not of a friction term or dissipative term at large scale.

The study of structure functions in the direct cascade range shows that the second order scaling exponent for increments perpendicular to the rotation in runs with small Ro is $\zeta_2 \approx 1$, in agreement with the evaluation of the energy spectrum spectral index. Low order moments follow the curve $\zeta_p = p/2$ but high order moments deviate from this law, an indication of intermittency. The level of intermittency in the direct cascade of energy, as measured by the exponent $\mu = 2\zeta_3 - \zeta_6$, is the same for runs with and without rotation. The spontaneous formation of strong gradients in the small scales is further confirmed by pdfs of the velocity increments and by visualization of regions of strong vorticity in the flow.

More separation of scales is needed to study the intermittency in the inverse cascade of energy. Because of its relation to small scale gradients, intermittency is believed to be associated only with the forward cascade of energy. The intermittency phenomenon is not observed in the velocity field in two dimensional turbulence for which the conservation of vorticity leads to an inverse energy cascade to the large scales [12, 13], although intermittency in the vorticity (which cascades directly to small scales) is observed. It is unclear how the dual cascade of energy (towards both small and large scales) in rotating turbulence affects the intermittency in the inverse cascade range. While intermittency is associated with small scale events, in many cases the strong events can affect the dynamics of the large scales, specially in systems close to criticality; as an example, intermittency is a possible explanation for the occurrence of extended minima in solar activity [18, 39]; it is also known to affect the transport of momentum in atmospheric surface layers [31].

Acknowledgments

The authors would like to express their gratitude to J.R. Herring and J.J. Tribbia for their careful reading of the manuscript. Computer time was provided by NCAR. PDM is a member of the Carrera del Investigador Científico of CONICET. AA acknowledges support from Observatoire de la Côte d'Azur and Rotary Club's district 1730. The NSF grant CMG-0327888 at NCAR supported this work in part. NCAR is sponsored by NSF. Three-dimensional visualizations of the flows were done using VAPOR, a software for interactive visualization and analysis of terascale datasets [20].

[1] Alexakis, A., Bigot, B., Politano, H., and Galtier, S. Anisotropic fluxes and nonlocal interactions in magnetohydrodynamic turbulence. *Phys. Rev. E 76* (2007), 056313.

[2] Alexakis, A., Mininni, P. D., and Pouquet, A. Imprint of large-scale flows on turbulence. *Phys. Rev. Lett. 95* (2005), 264503.

[3] Alexakis, A., Mininni, P. D., and Pouquet, A. Shell-to-shell energy transfer in magnetohydrodynamics. i. steady state turbulence. *Phys. Rev. E 72* (2005), 046301.

[4] Alexakis, A., Mininni, P. D., and Pouquet, A. On the inverse cascade of magnetic helicity. *Astrophys. J. 640* (2006), 335–343.

[5] Alexakis, A., Mininni, P. D., and Pouquet, A. Turbulent cascades, transfer, and scale interactions in magnetohydrodynamics. *New J. Phys. 9* (2007), 298.

[6] Babiano, A., Basdevant, C., Legras, B., and Sadourny, R. Vorticity and passive-scalar dynamics in two-dimensional turbulence. *J. Fluid Mech. 183* (1987), 379–397.

[7] Babin, A., Mahalov, A., and Nicolaenko, B. Global splitting, integrability and regularity of three-dimensional Euler and Navier-Stokes equations for uniformly rotating fluids. *Eur. J. Mech. B/Fluids 15* (1996), 291–300.

[8] Bardina, J., Ferziger, J. H., and Rogallo, R. S. Effect of rotation on isotropic turbulence: computation and modeling. *J. Fluid Mech. 154* (1985), 321–336.

[9] Bartello, P., Métais, O., and Lesieur, M. Coherent structures in rotating three-dimensional turbulence. *J. Fluid Mech. 273* (1994), 1–29.

[10] Bellet, F., Godeferd, F. S., and Scott, F. S. Wave turbulence in rapidly rotating flows. *J. Fluid Mech. 562* (2006), 83–121.

[11] Benzi, R., Patarnello, S., and Santangelo, P. On the statistical properties of two-dimensional decaying turbulence. *Europhys. Lett. 3* (1987), 811–818.

[12] Benzi, R., and Scardovelli, R. Intermittency of two-dimensional decaying turbulence. *Europhys. Lett. 29* (1995), 371–376.

[13] Boffetta, G. Energy and enstrophy fluxes in the double cascade of two-dimensional turbulence. *J. Fluid Mech. 589* (2007), 253–260.

[14] Brachet, M. E., Meneguzzi, M., , and Sulem, P. L. Small-scale dynamics of high-Reynolds-number two-dimensional turbulence. *Phys. Rev. Lett. 57* (1986), 683–686.

[15] Cambon, C., and Jacquin, L. Spectral approach to non-isotropic turbulence subjected to rotation. *J. Fluid Mech. 202* (1989), 295–317.

[16] Cambon, C., Mansour, N. N., and Godeferd, F. S. Energy transfer in rotating turbulence. *J. Fluid Mech. 337* (1997), 303–332.

[17] Canuto, V. M., and Dubovikov, M. S. A dynamical model for turbulence. V. The effect of rotation. *Phys. Fluids 9* (1997), 2132–2140.

[18] Charbonneau, P. Multiperiodicity, chaos, and intermittency in a reduced model of the solar cycle. *Sol. Phys. 199* (2001), 385–404.

[19] Chen, Q., Chen, S., Eyink, G. L., and Holm, D. Resonant interactions in rotating homogeneous three-dimensional turbulence. *J. Fluid Mech. 542* (2005), 139–164.

[20] Clyne, J., Mininni, P., Norton, A., and Rast, M. Interactive desktop analysis of high resolution simulations: application to turbulent plume dynamics and current sheet formation. *New J. Phys. 9* (2007), 301.

[21] Domaradzki, J. A. Analysis of energy transfer in direct numerical simulations of isotropic turbulence. *Phys. Fluids 31* (1988), 2747–2749.

[22] Domaradzki, J. A., and Rogallo, R. S. Local energy transfer and nonlocal interactions in homogeneous, isotropic turbulence. *Phys. Fluids A 2* (1990), 413–426.

[23] Embid, P. F., and Majda, A. Averaging over fast gravity waves for geophysics flows with arbitrary potential vorticity. *Commun. Partial Diff. Equat. 21* (1996), 619–658.

[24] Frisch, U. *Turbulence: the legacy of A.N. Kolmogorov.* Cambridge Univ. Press, Cambridge, 1995.

[25] Galtier, S. Weak inertial-wave turbulence theory. *Phys. Rev. E 68* (2003), 015301.

[26] Greenspan, H. P. *The theory of rotating fluids.* Cambridge Univ. Press, Cambridge, 1968.

[27] Hossain, M. Reduction in the dimensionality of turbulence due to a strong rotation. *Phys. Fluids 6* (1994), 1077–1080.

[28] Iroshnikov, P. S. Turbulence of a conducting fluid in a strong magnetic field. *Sov. Astron. 7* (1963), 566–571.

[29] Jacquin, L., Leuchter, O., Cambon, C., and Mathieu, J. Homogeneous turbulence in the presence of rotation. *J. Fluid Mech. 220* (1990), 1–52.

[30] Kraichnan, R. H. Inertial-range spectrum of hydromagnetic turbulence. *Phys. Fluids 8* (1965), 1385–1387.

[31] Kulkarni, J. R., Sadani, L. K., and Murthy, B. S. Wavelet analysis of intermittent turbulent transport in the atmospheric surface layer over a monsoon trough region. *Bound.-Layer Meteor. 90* (1999), 217–239.

[32] Liechtenstein, L., Godeferd, F. S., and Cambon, C. Nonlinear formation of structures in rotating stratified turbulence. *J. of Turbulence 6* (2005), N24.

[33] Maltrud, M. E., and Vallis, G. K. Energy spectra and coherent structures in forced two-dimensional and beta-plane turbulence. *J. Fluid Mech. 228* (1991), 321–342.

[34] McWilliams, J. C. The emergence of isolated coherent vortices in turbulent flow. *J. Fluid Mech. 146* (1984), 21–43.

[35] Miesch, M. S., Elliott, J. R., Clune, J. T. T. L., Glatzmaier, G. A., and Gilman, P. A. Three-dimensional spherical simulations of solar convection. I. Differential rotation and pattern evolution achieved with laminar and turbulent states. *Astrophys. J. 532* (1999), 593–615.

[36] Milano, L. J., Matthaeus, W. H., Dmitruk, P., and Montgomery, D. C. Local anisotropy in incompressible magnetohydrodynamic turbulence. *Phys. Plasmas 8* (2001), 2673–2681.

[37] Mininni, P. D., Alexakis, A., and Pouquet, A. Shell-to-shell energy transfer in magnetohydrodynamics. ii. kinematic dynamo. *Phys. Rev. E 72* (2005), 046302.

[38] Mininni, P. D., Alexakis, A., and Pouquet, A. Large-scale flow effects, energy transfer, and self-similarity on turbulence. *Phys. Rev. E 74* (2006), 016303.

[39] Mininni, P. D., Gómez, D. O., and Mindlin, G. B. Biorthogonal decomposition techniques unveil the nature of the irregularities observed in the solar cycle. *Phys. Rev. Lett. 89* (2002), 061101.

[40] Mininni, P. D., and Pouquet, A. Energy spectra stemming from interactions of Alfvén waves and turbulent eddies. *Phys. Rev. Lett. 99* (2007), 254502.

[41] Mininni, P. D., Alexakis, A., and Pouquet, A. Nonlocal interactions in hydrodynamic turbulence at high Reynolds numbers: The slow emergence of scaling laws. *Phys. Rev. E 77* (2008), 036306.

[42] Monchaux, R., Berhanu, M., Bourgoin, M., Moulin, M., Odier, Ph., Pinton, J.-F., Volk, R., Fauve, S., Mordant, N., Pétrélis, F., Chiffaudel, A., Daviaud, F., Dubrulle, B., Gasquet, C., Marié, L., and Ravelet, F. Generation of a magnetic field by dynamo action in a turbulent flow of liquid sodium. *Phys. Rev. Lett. 98* (2007), 044502.

[43] Morf, R. H., Orszag, S. A., and Frisch, U. Spontaneous singularity in three-dimensional, inviscid, incompressible flow. *Phys. Rev. Lett. 44* (1980), 572–575.

[44] Morinishi, Y., Nakabayashi, K., and Ren, S. Dynamics of anisotropy on decaying homogeneous turbulence subjected to system rotation. *Phys. Fluids 13* (2001), 2912–2922.

[45] Müller, W.-C., and Thiele, M. Scaling and energy transfer in rotating turbulence. *Europhys. Lett. 77* (2007), 34003.

[46] Pedlosky, J. *Geophysical fluid dynamics.* Springer, Berlin, 1986.

[47] Sagaut, P., and Cambon, C. *Homogeneous turbulence dynamics.* Cambridge Univ. Press, Cambridge, 2008.

[48] She, Z. S., and Lévêque, E. Universal scaling laws in fully developed turbulence. *Phys. Rev. Lett. 72*, 3 (1994), 336–339.

[49] Shebalin, J. V. Matthaeus, W. H., and Montgomery, D. Anisotropy in MHD turbulence due to a mean magnetic field. *J. Plasma Phys. 29* (1983), 525–547.

[50] Simand, C., Chillà, F., and Pinton, J.-F. Study of inhomogeneous turbulence in the closed flow between corotating disks. *Europhys. Lett. 49* (2000), 336–342.

[51] Smith, L. M., Chasnov, J. R., and Waleffe, F. Crossover from two- to three-dimensional turbulence. *Phys. Rev. Lett. 77* (1996), 2467–2470.

[52] Smith, L. M., and Lee, Y. On near resonances and symmetry breaking in forced rotating flows at moderate rossby number. *J. Fluid Mech. 535* (2005), 111–142.

[53] Smith, L. M., and Waleffe, F. Transfer of energy to two-dimensional large scales in forced, rotating three-dimensional turbulence. *Phys. Fluids 11* (1999), 1608–1622.

[54] Staplehurst, P.J., Davidson, P.A., and Dalziel, S.B. Structure formation in homogeneous freely decaying rotating turbulence. *J. Fluid Mech. 598* (2008), 81–105.

[55] Taylor, G. I., and Green, A. E. Mechanism of the production of small eddies from large ones. *Proc. Roy. Soc. Lond. Ser. A 158*, 895 (Feb 1937), 499–512.

[56] van Bokhoven, L. J. A., Cambon, C., Liechtenstein, L., Godeferd, F. S., and Clercx, H. J. H. Refined vorticity statistics of decaying rotating three-dimensional turbulence. *J. of Turbulence 9* (2008), N6.

[57] Waleffe, F. Inertial transfers in the helical decomposition. *Phys. Fluids A 5* (1993), 677–685.

[58] Yang, X., and Domaradzki, J. A. LES of decaying rotating turbulence. *Phys. Fluids 16* (2004), 4088–4104.

[59] Yeung, P. K., and Zhou, Y. Numerical study of rotating

turbulence with external forcing. *Phys. Fluids 10* (1998), 2895–2909.

[60] Zeman, O. A note on the spectra and decay of rotating homogeneous turbulence. *Phys. Fluids 6* (1994), 3221–3223.

[61] Zhou, Y. A phenomenological treatment of rotating turbulence. *Phys. Fluids 7* (1995), 2092–2094.